Ice sheet–derived submarine groundwater discharge on Greenland's continental shelf

Whitney DeFoor,[1] Mark Person,[1] Hans Christian Larsen,[2] Daniel Lizarralde,[3] Denis Cohen,[4] and Brandon Dugan[5]

Received 11 February 2011; revised 3 June 2011; accepted 13 June 2011; published 28 July 2011.

[1] Isotopically light (−1‰ to −8‰ $\delta^{18}O$) and fresh pore fluids (300–520 mM Cl^-) were found in continental shelf sediments up to 100 km offshore of southeastern (SE) Greenland, suggesting infiltration and mixing of ice sheet meltwater with seawater to depths of 260 m. These geochemical anomalies may be associated with ice sheet–derived submarine groundwater discharge (SMGD). We present a continental-scale reconstruction of the late Pleistocene hydrogeology of SE Greenland using finite element analysis that incorporates ice sheet loading and solute and isotope transport. Results indicate that subglacial infiltration and SMGD are of the same order of magnitude and are highly dependent on the permeability of the subaerial basalt. Simulated infiltration and SMGD almost doubled during the Last Glacial Maximum, compared to ice-free conditions. Much of the present-day glacially induced groundwater discharge occurs on land. Subice infiltration on the continental shelf likely represents a mixture of seawater and meltwater during past glacial maximums. Simulated SMGD during the most recent interval of glacial retreat is about 4% of the total ice sheet melting. At present, the simulated rate of SMGD is about 11% of the estimated current melting rate.

Citation: DeFoor, W., M. Person, H. C. Larsen, D. Lizarralde, D. Cohen, and B. Dugan (2011), Ice sheet–derived submarine groundwater discharge on Greenland's continental shelf, *Water Resour. Res., 47*, W07549, doi:10.1029/2011WR010536.

1. Introduction

[2] Paleohydrologic reconstructions of North America's Laurentide ice sheet suggest that high recharge rates, up to 10 times modern values, occurred when wet-based ice sheets overran the North American craton and continental shelf [*Person et al.*, 2003, 2007]. Between 15% and 70% of basal meltwater from the Laurentide ice sheet may have infiltrated the Canadian Shield and sedimentary basins of North America [*Lemieux et al.*, 2008]. This has important implications for understanding ice sheet dynamics [*Flowers et al.*, 2005; *Le Brocq et al.*, 2009], assessing long-term (10^6 years) safety of high-level nuclear waste repositories in Canada and northern Europe [*Talbot*, 1999], understanding continental-scale hydrologic budgets of modern ice sheets, such as Greenland [*Makahnouk et al.*, 2009], and understanding submarine groundwater effects on biogeochemical cycles [*McIntosh et al.*, 2002].

[3] Sediment pore fluids collected offshore southeastern (SE) Greenland at Ocean Drilling Program (ODP) Leg 152 Sites 914–916 and 918 suggest that subglacial meltwater has infiltrated into continental shelf sediments. It is unclear whether or not this same infiltration is occurring today via deep aquifer systems. These ODP sites were drilled between 40 and 100 km offshore SE Greenland (Figures 1a and 1c). The pore fluids found at these sites have chloride concentrations and oxygen isotope compositions that indicate mixing between seawater (0‰ $\delta^{18}O$, 535 m*M* Cl^-) and isotopically depleted subglacial meltwaters (−40‰ $\delta^{18}O$, 0 m*M* Cl^-; circles in Figure 1b) to depths of at least 260 m [*Gieskes et al.*, 1998; *Makahnouk*, 2009]. Sites 914–916 are located in the continental shelf sediments, and Site 918 is in the near-ocean basin. The presence of fresh and isotopically light pore fluids in continental shelf sediments recovered from SE Greenland raises several questions: How might subglacial meltwater have penetrated so far offshore? What role has expansion and contraction of the Greenland ice sheet played in subglacial and continental shelf hydrogeology? Were the pore fluids emplaced by downward infiltration through continental shelf sediments and tills during the Last Glacial Maximum (LGM) or by upward discharge through deep underlying basalt aquifers?

[4] Geophysical data and discoveries of glacial deposits on the continental shelf indicate that Greenland's ice sheet extended to the shelf-slope break during the LGM [*Larsen et al.*, 1998]. This would have provided direct access of

[1]Hydrology Program, Department of Earth and Environmental Science, New Mexico Institute of Mining and Technology, Socorro, New Mexico, USA.
[2]Office of Liaison and Cooperative Research, Integrated Ocean Drilling Program, Inc., Tokyo University of Marine Science and Technology, Tokyo, Japan.
[3]Department of Geology and Geophysics, Woods Hole Oceanographic Institution, Woods Hole, Massachusetts, USA.
[4]Department of Geological and Atmospheric Science, Iowa State University, Ames, Iowa, USA.
[5]Department of Earth Science, Rice University, Houston, Texas, USA.

0043-1397/11/2011WR010536

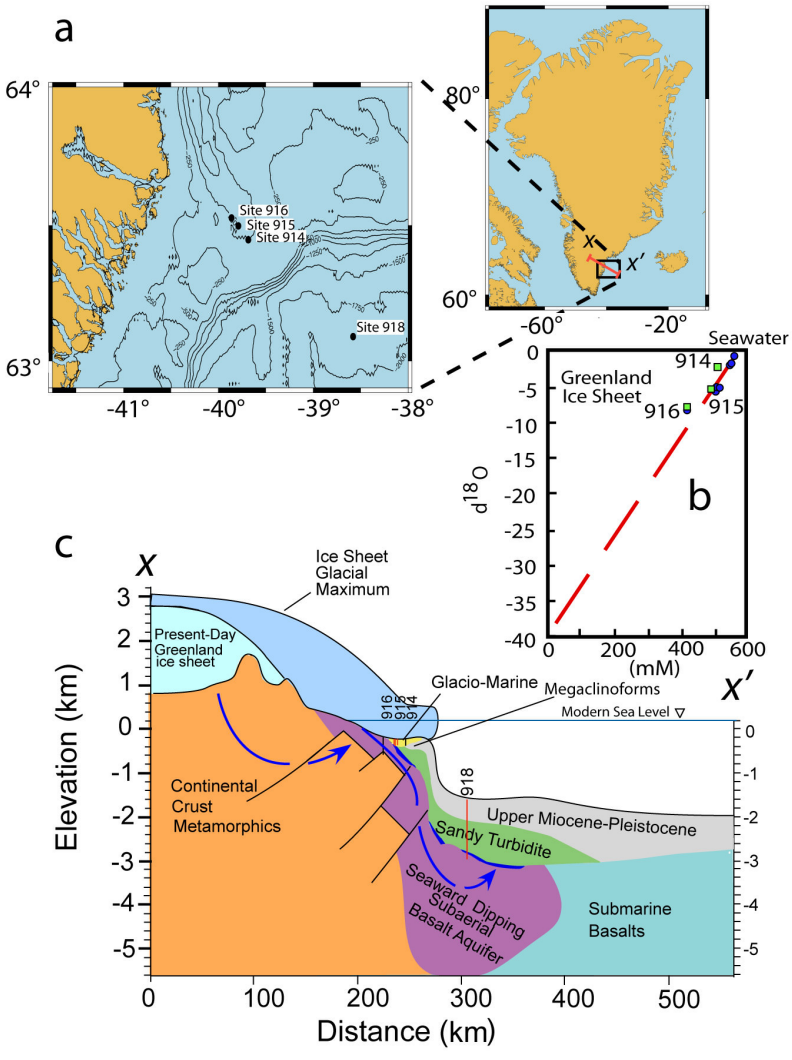

Figure 1. (a) Map of Leg 152 well sites [*Larsen et al.*, 1998] with bathymetry. (b) Scattergram plot of minimum pore water $\delta^{18}O$ and Cl^- composition for different ODP test wells. Green squares are simulation results from the cross-sectional paleohydrologic model, and blue circle are observations from ODP Leg 152 wells [*Gieskes et al.*, 1998]. The red dashed line is the mixing line between seawater and Greenland glacial meltwater. (c) Hydrostratigraphic representation of SE Greenland used in paleohydrogeologic model reconstruction. The location of the *x* section is shown in Figure 1a. The vertical red lines near sediment-water interface are approximate locations of ODP test well sites. Blue arrows denote inferred groundwater flow directions. A thin (125 m) till layer, although present in the model, is not shown in Figure 1c.

meltwater to the continental shelf-slope sediment pores via vertical downward infiltration, possibly contributing to freshening of the sediment pore fluids observed in the ODP wells [*Cohen et al.*, 2009]. Presently, the Greenland ice sheet creates a hydraulic head gradient between the coast and the continent of about 0.014, assuming hydraulic head that is 90% of the ice sheet thickness [*Parizek and Alley*, 2004] (Figure 1c). If the ice sheet was removed and the topography of SE Greenland remained, the gradient would decrease by a factor of 3, to 0.0056 [*Larsen et al.*, 1998]. Near the edge of the ice sheet, groundwater discharges upward, potentially transporting glacial meltwater upward. The ice sheet–induced hydraulic head gradient may also direct infiltrating meltwater into deep aquifer units, which could migrate offshore (Figure 1c). Groundwater flow from beneath Greenland's present-day ice sheet to the ocean must traverse a thick sequence of Proterozoic metamorphic rocks, seaward dipping igneous rocks, and continental shelf sediments [*Larsen et al.*, 1998] (Figure 1c). A portion of subglacial-derived meltwater also likely discharges just beyond the toe of the ice sheet, contributing base flow to surface water bodies such as taliks. While the role of ice sheet loading on subsurface flow has recently been considered on Iceland and Antarctica [*Flowers et al.*, 2005; *Le Brocq* et al., 2009], this is the first study to address hydrogeologic connections between continental and marine realms associated with the Greenland ice sheet.

[5] This study investigates connections between subglacial infiltration, groundwater discharge, and pore fluid chemistry on SE Greenland's continental shelf. One of the main goals of this study is to gain knowledge about the role

of groundwater in the continental-scale hydrologic budget of SE Greenland, past and present. This study also attempts to address whether or not modern groundwater flow patterns could be responsible for pore fluid chemistry at ODP wells. Finally, we wish to determine whether or not submarine groundwater discharge (SMGD) contributes to sea level rise because of ice sheet melting and whether the SMGD could have a role in biogeochemical processes on the continental shelf, both in the past and present. To address these issues, we developed a continental-scale, two-dimensional, paleohydrologic model. Using this model, we conducted a sensitivity study to reconstruct infiltration and discharge fluxes and pore water chemistry on SE Greenland.

[6] We review the initial conditions and boundary conditions we used in our modeling exercise. Appendix A contains a summary of the mathematical model assumptions and transport equations used. We varied till and bedrock aquifer permeability because of the paucity of permeability data for Greenland to estimate a reasonable range of hydraulic parameters. As part of the sensitivity study, we also varied the salinity and isotropic composition along the top boundary at the base of the ice sheet on the continental shelf to account for the influence of mixing between marine and meltwater fluid sources.

2. Study Site

[7] The presence of the Greenland ice sheet makes accurate characterization of Greenland's geology and hydrogeologic setting difficult. Core and geophysical data provide some information about SE Greenland geologic units [*Hopper et al.*, 2003; *Larsen et al.*, 1998]. SE Greenland's continental crust is dominantly composed of Precambrian metamorphic rocks, which are covered by Cretaceous seaward dipping subaerial basalts [*Larsen et al.*, 1998]. SE Greenland's continental shelf contains late Neogene and Quaternary sediments, glaciomarine deposits, megaclinoforms, and a layer of glacial tills. Turbidite deposits and upper Miocene-Pliocene marine sediments are present under the continental shelf sediments and extend into the ocean basin. Cretaceous submarine basalts are adjacent to the subaerial basalts [*Larsen et al.*, 1998] (Figure 1c). Submarine basalts are basalts formed underwater, such as along mid-ocean ridges. Subaerial basalts are basalts that solidify under the air, likely originating from lava flows.

[8] Ice sheet models predict that the Greenland ice sheet thickness varied from 0 m (~140–114 ka; Eemian Interglacial) to 3000 m (~20 ka) near the center of the continent [*Cuffey and Marshall*, 2000; *Parizek and Alley*, 2004] (Figure 1c). The ice sheet likely extended onto the continental shelf slope at ~20 ka (Last Glacial Maximum). Note that the term "glacial maximums" represents periods at which the ice sheet was large and near its largest and the term "interglacials" represents a period in which the ice sheet was small and/or not present.

3. Methods

[9] In order to characterize Greenland's present-day hydrology and paleohydrology, we sequentially solved two-dimensional, transient, variable density groundwater flow, heat, and solute transport equations using the finite element method. The advective-dispersive solute and isotope ($\delta^{18}O$) transport was solved using a Lagrangian-based modified method of characteristics. Our numerical methods are described in detail in Appendix A. Table 1 contains the parameters we used.

Table 1. Parameters Used in All Simulations

Model Parameters	Symbols	Value
Water density at standard conditions[a]	ρ_o	1000 kg m^{-3}
Density of ice	ρ_i	916 kg m^{-3}
Density of rock	ρ_s	2675 kg m^{-3}
Specific heat capacity of rock	c_f	4187 Cal kg^{-1} °C^{-1}
Triple point temperature of water	T_{TP}	0.0098°C
Ice thermal diffusivity	κ	37.2 m^2 yr^{-1}
Basal temperature gradient	β_b	0.02°C m^{-1}
Atmospheric lapse rate	λ	−0.007°C m^{-1}
Water melting point depression	c_i	0.0861 K MPa^{-1}

[a]Standard conditions are 10°C, 0.0 mass fraction salinity, and 0.0 MPa.

3.1. Model Domain

[10] Our cross-sectional hydrogeological model extends from the continental interior of SE Greenland to about 600 km to the east (about 400 km east of the modern shoreline) and to a depth of about 5.5 km under the continental shelf (Figure 1c). We used three node triangular elements and a linear approximation function in our finite element model. The mesh had 14,160 elements and 7259 nodes. We refined the top 1300 m of the mesh using a 50 m vertical spacing between nodes. All simulations were run for 1.05 Myr (~10 glacial cycles), with a time step size of 10 years.

3.2. Head Boundary Conditions

[11] The sides and bottom of the model domain were prescribed no-flow boundaries for groundwater flow. Hydraulic head at the top boundary was fixed. In areas overrun by the ice sheet, we increased hydraulic head by adding 90% of the approximated ice sheet thickness to the rock surface elevation. This assumes Greenland's ice sheet has sufficient basal and surface meltwater generation rates to keep fluid pressures at or near floating conditions. The validation of this assumption is supported by pore pressure reconstruction from under consolidated tills [*Hooyer and Iverson*, 2002], as well as fluid pressure measurements beneath modern ice sheets [*Engelhardt and Kamb*, 1997]. As discussed in section 3.6, this condition is modified where permafrost is present. Subaerial nodes not covered by the ice sheet were given heads equal to the land surface elevation, and nodes below sea level were given heads equal to sea level elevation corrected for seawater density.

[12] We approximated the ice sheet thickness (x) using a polynomial similar to the one presented by *Vialov* [1958],

$$\eta(x) = H_t\sqrt{\left|1.0 - (x/L_t)^2\right|}, \tag{1}$$

where H_t is the thickness of the ice sheet at the summit, L_t is the extent of the ice sheet from its center, and x is the distance from the summit (center) of the ice sheet. Waxing and waning of the ice sheet throughout the ten 100 kyr glacial cycles was simulated by having the ice sheet height rise to 3 km and extend to the continental shelf-slope break over 75 kyr and then retreat over 25 kyr. This trend varied from 22 ka to the present in order that the ice sheet matched

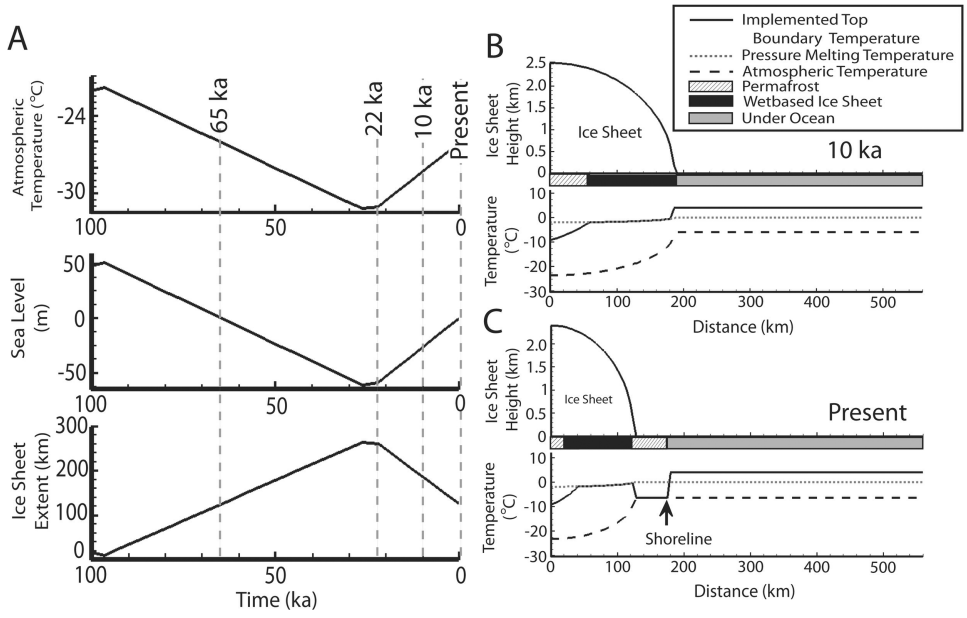

Figure 2. Imposed hydrologic, chemical, and thermal boundary conditions, 100 ka to present day. (a) Assumed changes in atmospheric temperature, sea level, and ice sheet extent during the last 100 kyr for SE Greenland. Atmospheric temperature along with a lapse rate was used to calculate the temperature along the top of the ice sheet and land surface. Below sea level, we specified a freshwater head equal to sea level elevation, accounting for the added weight of seawater. Ice sheet extent, location of permafrost, and sub-sea level position at (b) 10 ka and (c) present day. Boundary nodes underneath the ice sheet were assigned heads equal to the node elevation plus 90% of the ice sheet thickness. Except for the last 22 kyr, the ice sheet decreased from its maximum size (270 km long and 3 km tall) to its minimum size (0 km long and 0 km tall) over 25 kyr. For land surface nodes beneath the ice sheet, the imposed temperature was calculated using a one-dimensional advective-conductive analytical solution. Ice-free areas along the top boundary were set to the atmospheric temperature. Boundary nodes below sea level were assigned a temperature of 4°C. When the land surface temperature was less than the pressure melting temperature, we accounted for the presence of permafrost by decreasing the permeability of land surface elements by 2 orders of magnitude.

the present ice sheet size today (Figure 2a). We did not model the ice sheet dynamics. Instead, we imposed a time-dependent load on the model domain and top boundary that increased the head where the load was present.

3.3. Thermal Boundary Conditions and Initial Conditions

[13] For heat transfer, we imposed an insulated side boundary condition and an initial depth-dependent temperature profile of 30°C km^{-1}. At the base of the model we imposed a basal heat flux of 0.06 W m^{-2}, which is typical for the continental crust. At the top boundary a temperature of 4°C was specified for all surface nodes below sea level (Figures 2b and 2c). Subaerial surfaces were set to estimated air temperature on the basis of ice core records [*Imbrie et al.*, 1984; *Johnsen et al.*, 1995]. We incorporated paleotemperature and sea level data determined from ocean $\delta^{18}O$ sediment records and from Greenland Ice Core Project (GRIP) ice core records [*Johnsen et al.*, 1995; *Imbrie et al.*, 1984] in order to reconstruct paleoclimatic data. The sediment data sets show that temperature varied by 10°C and sea level varied by ~110 m between glacial maximums and glacial minimums. We shifted the paleotemperatures to match Greenland ice sheet summit temperatures [*Dahl-Jensen*, 1998; *Johnsen et al.*, 1995] (Figure 2a). We then used a lapse rate of −0.007°C m^{-1} [*Hanna et al.*, 2005] to determine the air temperature with decreasing elevation (Figures 2b and 2c).

3.4. Ice Sheet Heat Basal Temperature

[14] The presence of permafrost can cause large reductions in permeability [*McKenzie et al.*, 2007]. Thus, approximating temperatures under the ice sheet was important for our hydrologic model. Temperatures within and at the base of ice sheets are controlled by both conduction and advection. When the ice sheet was present, we used a one-dimensional analytical solution for advective-conductive transport to calculate the basal temperature of the ice sheet and then applied this temperature to the surface nodes under the ice sheet in our model (Figures 2b and 2c). The analytical solution used is described in detail in Appendix B.

3.5. Salinity and $\delta^{18}O$ Boundary and Initial Conditions

[15] Beneath the onshore segment of SE Greenland we imposed an initial vertical salinity gradient of 5.0×10^{-6} mass fraction m^{-1} and temperature-dependant equilibrium $\delta^{18}O$ concentrations. This resulted in a basal concentration of about 0.025 mass fraction. Offshore segments were initially prescribed a salinity of 0.035 mass fraction and 0‰

$\delta^{18}O$. The top boundary conditions for solute transport equations were a constant concentration of 0.0 mass fraction for surface nodes above sea level and beneath the ice sheet and 0.035 mass fraction for surface nodes below sea level. The concentration of $\delta^{18}O$ at the top boundary nodes was set to 0‰ when below sea level, −40‰ when below the ice sheet, and −10‰ when subaerial. We ran simulations with the top boundary conditions on the continental shelf assuming a mixture of seawater and glacial meltwater. We considered two scenarios for specifying the upper isotopic and salinity boundary conditions beneath Greenland's ice sheet on the continental shelf: (1) −40‰ $\delta^{18}O$ and 0 mass fraction salinity (100% meltwater) and (2) −3‰ $\delta^{18}O$ and 0.0315 mass fraction salinity (93% seawater and 7% meltwater) (Figure 1c). As shown in section 4.1, a close match between modeled and observed salinity and oxygen isotope results could not be achieved without mixing of seawater and meltwater at the base of the ice sheet.

3.6. Permeability and Permafrost Effects

[16] The permeabilities for the different lithologic units we used in our model are presented in Table 2. The permeability of Greenland's crustal rocks is not well known. Hydrothermal modeling suggests that the metamorphic crustal rocks are hydrologically tight [*Norton and Taylor*, 1979]. Other studies, however, suggest that permeability of crystalline rock is high toward the surface ($\sim 10^{-13}$ m^2) and then decreases with depth [*Ingebritsen and Manning*, 1999]. Overlying the outer edge of the continent are late Neogene subaerial and submarine basalts [*Hopper et al.*, 2003]. Similar subaerial basalts in Hawaii have horizontal permeability that range from 10^{-14} and 10^{-11} m^2 [*Gingerich*, 1999] and are 10–1000 times greater than vertical permeabilities [*Souza and Voss*, 1987]. Submarine basalt has an in situ permeability that typically ranges from 10^{-18} to 10^{-10} m^2 [*Fisher*, 1998; *Fisher et al.*, 2008]. Sedimentary deposits covering the basalts on the continental shelf could have permeabilities that range from 10^{-13} to 10^{-16} m^2 for sandy sediments and from 10^{-14} to 10^{-18} m^2 for fine-grained sediments [*Spinelli et al.*, 2004]. Tills generally have low permeabilities, typically less than 10^{-16} m^2 [*Gerber and Howard*, 2000; *Keller et al.*, 1989], though fractures and heterogeneities within tills can increase till permeability upward of 10^{-12} m^2 [*Gerber and Howard*, 2000]. Permafrost can decrease permeability by orders of magnitude [*McKenzie et al.*, 2007].

[17] Permeability was decreased by a factor of 100 if the temperature of an element was below the pressure melting temperature in order to represent permafrost [*McKenzie et al.*, 2007] (Figures 2b and 2c). The parameters that were held constant for all units and all simulations, which we did not attempt to optimize, included longitudinal dispersivity (1000 m), transverse dispersivity (100 m), and solute diffusivity (3.5×10^{-10} m^2 s^{-1}). During the first glacial cycle we deposited a low-permeability till on the continental shelf, which remained throughout the model simulation. The till was about 100 m thick.

3.7. Sensitivity Study

[18] We conducted a sensitivity study varying the permeability of the tills and subaerial basalts as well as changing the continental shelf meltwater composition along the top boundary. We compared model results to pore fluid chemistry at ODP Leg 152 Sites 914–916 and 918. As part of the sensitivity study we calculated subglacial infiltration, SMGD, and subaerial discharge rates.

[19] First, we investigated the effects of subaerial basalt and till permeability on simulated pore fluid chemistry at the ODP Leg 152 sites. We ran simulations with the permeability of the subaerial basalt varying between 10^{-15} and 10^{-12} m^2, with the continental shelf ice boundary condition at 100% meltwater. We then ran a series of simulations in which we varied the till permeability between 10^{-19} and 10^{-17} m^2, also with the continental shelf ice boundary condition at 100% meltwater. We repeated the simulations with varying subaerial basalt permeability, except the boundary condition on the continental shelf was changed to 0.0315 mass fraction salinity and −3‰ $\delta^{18}O$ (93% seawater and 7% meltwater) when the ice sheet was over the shelf. Units whose permeability were not varied in a given sensitivity study were given permeabilities in Table 2. We varied the permeabilities of Precambrian metamorphic rock, submarine basalt, upper Miocene–Pleistocene sediments, and turbidities and found that they did not have a large effect on calculated salinity and $\delta^{18}O$ composition when they were varied within their range of uncertainty. In total, our sensitivity study included five permeability scenarios and two boundary condition scenarios (Table 3). The scenarios are designated with SN and a number. We then chose a best fit scenario (BFS) to do a more in depth analysis of the past and present glacially influenced hydrogeology of SE Greenland.

4. Results

[20] Here we present the results of our sensitivity study and a more in depth analysis of our BFS. All simulations ran for 1.05 Myr ($\sim$10 glacial cycles). Our primary means of comparison between scenarios were plots of computed

Table 2. Hydrogeologic Properties Assigned in the Paleohydrologic Model

Unit	k_{max}[a] (m^2)	ϕ[b]	S_s[c] (m^{-1})	Permeability References
Precambrian metamorphic	10^{-14}–10^{-19}	0.1	0	*Ingebritsen and Manning* [1999], *Norton and Taylor* [1979]
Oceanic basalts	10^{-16}	0.05	10^{-7}	*Fisher* [1998]
Subaerial basalts	10^{-13}	0.1	10^{-5}	*Izuka and Gingerich* [2003], *Souza and Voss* [1987]
Turbidites	10^{-16}	0.2	10^{-6}	*Spinelli et al.* [2004]
Pleistocene sediments	10^{-14}	0.3	10^{-4}	*Spinelli et al.* [2004]
Megaclinoforms	10^{-14}	0.3	10^{-5}	*Spinelli et al.* [2004]
Glaciomarine	10^{-14}	0.3	10^{-4}	*Spinelli et al.* [2004]

[a]Permeability.
[b]Porosity.
[c]Specific storage coefficient.

Table 3. Subaerial Basalt and Till Permeabilities and Boundary Conditions Assigned for the Sensitivity Study Scenarios

Sensitivity Study Scenarios	Subaerial Basalt k_{max} (m^2)	Till k_{max} (m^2)	Salinity Boundary Condition (mmol)	$\delta^{18}O$ Boundary Condition (‰)
SN1	10^{-13}	10^{-17}	0	−40
SN2	10^{-14}	10^{-17}	0	−40
SN3	10^{-12}	10^{-17}	0	−40
SN4	10^{-13}	10^{-18}	0	−40
SN5	10^{-13}	10^{-19}	0	−40
SN6	10^{-13}	10^{-17}	0.0315	−3
SN7	10^{-14}	10^{-17}	0.0315	−3
SN8	10^{-12}	10^{-17}	0.0315	−3

versus observed salinity-depth data from the ODP wells (Figure 3).

4.1. Sensitivity Study

4.1.1. Subaerial Basalt Permeability

[21] Subaerial basalt horizontal permeability (K_x) was varied between 10^{-14} and 10^{-12} m^2 (SN1–SN3; Table 3). In all simulations, the subaerial basalt had an anisotropy (K_x/K_z) of 10. Calculated modern pore fluid chemistry for IODP wells had a tendency to be highly freshened by ice sheet loading (Figure 3a). Ice sheet loading caused meltwater to move both down (from beneath the ice sheet) and laterally (from the subaerial basalt) into the continental shelf sediments. With continental shelf ice boundary conditions at 100% meltwater, decreasing subaerial basalt permeability retarded meltwater infiltration into continental shelf units (Figure 3a) and produced simulated pore fluid chemistry closer to, though not consistent with, observed data.

[22] For all subaerial basalt permeability scenarios (SN1–SN3 and SN6–SN8), simulated pore fluid chemistry for Site 916 was more consistent with observed data than simulated data at Sites 914–915. As mentioned, glacial loading caused infiltrating water to enter the continental shelf sediment both laterally and downward vertically.

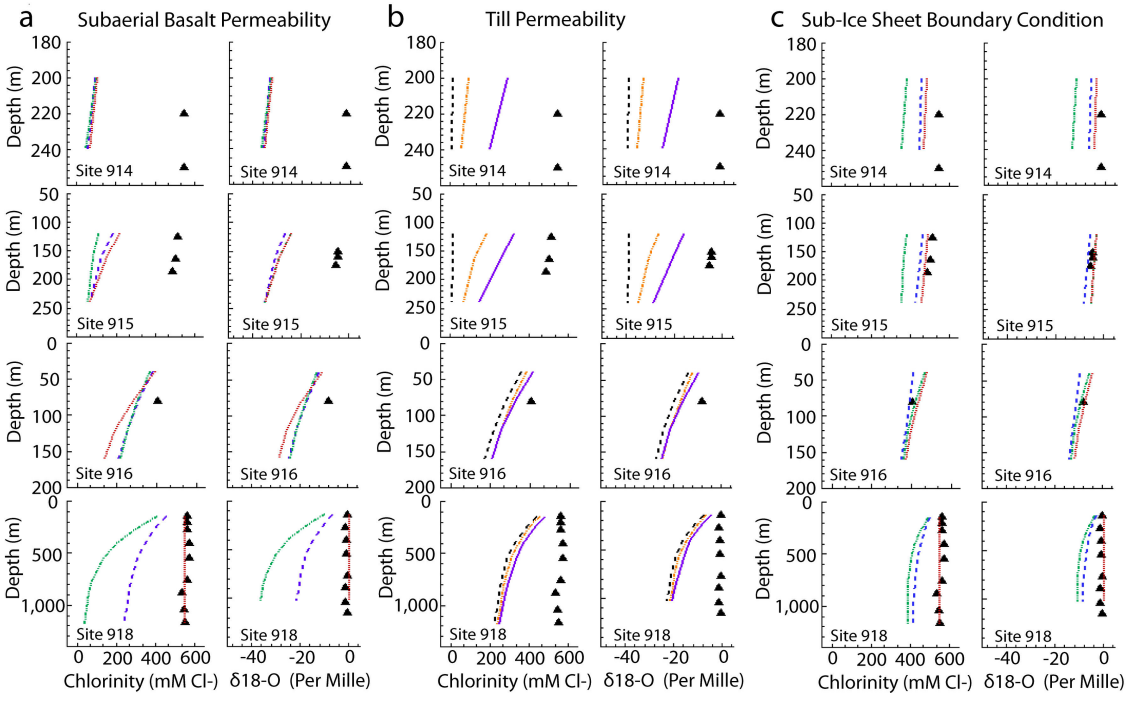

Figure 3. Comparison of simulated (lines) and observed (triangles) groundwater salinity and $\delta^{18}O$ composition from the sensitivity study in which permeability and imposed upper isotopic boundary conditions were varied. The $\delta^{18}O$ and chlorinity values are from ODP Leg 152 Sites 914–916 and 918 test wells. Computed results are from nodes located at respective ODP wells. (a) Varying subaerial basalt permeabilities, assuming anisotropy (K_x/K_z) of 10, with 100% meltwater boundary condition beneath the ice sheet (−40‰ $\delta^{18}O$, 0 mass fraction salinity). Red dotted line, $K_x = 10^{-14}$ m^2; blue dashed line, $K_x = 10^{-13}$ m^2; green dash-dotted line, $K_x = 10^{-12}$ m^2. Till permeability is 10^{-17} m^2 (b) Varying till permeabilities, assuming isotropic conditions, with 100% meltwater boundary condition. Orange dash-dotted line, $K_x = 10^{-17}$ m^2; purple solid line, $K_x = 10^{-13}$ m^2; black dashed line, $K_x = 10^{-19}$ m^2. Subaerial basalt permeability is 10^{-13} m^2. (c) Varying subaerial basalt permeabilities, as in Figure 3a, with 93% seawater and 7% meltwater boundary condition (−3‰ $\delta^{18}O$ and 0.0315 mass fraction salinity). Red dotted line, $K_x = 10^{-14}$ m^2; blue dashed line, $K_x = 10^{-13}$ m^2; green dash-dotted line, $K_x = 10^{-12}$ m^2. Till permeability is 10^{-17} m^2.

Low-permeability (10^{-17} m^2) till deposited on top of continental shelf sediments retarded vertical infiltration of seawater. However, outcropping subaerial basalt provided a path for infiltrating seawater to alter previously freshened pore chemistry in adjacent continental shelf sediments. In our model, Site 916 is right at the boundary between continental shelf sediments and subaerial basalt (Figure 1c), and thus its simulated pore chemistry is more affected by infiltrating seawater. The height of the sea level column, inducing seawater infiltration, was not high enough to focus seawater downward through the till to alter simulated pore chemistry at Sites 914 and 915. Best fit simulated pore chemistry at Site 918 indicates that subaerial basalt permeability is about 10^{-14} m^2.

4.1.2. Till Permeability

[23] Varying till permeability (10^{-13}–10^{-19} m^2) indicates that lower till permeability decreased the ability for seawater to enter continental shelf sediments via the seafloor and reduce meltwater induced freshening of continental shelf pore fluids (Figure 3b). Subaerial basalt permeability was 10^{-13} m^2 during these simulations. Over the continental shelf, simulated ice sheet–induced heads during glacial maximums are greater than simulated seawater-induced heads during sea level highstands (glacial minimums). Ice sheet loading allowed for more infiltration of fresh meltwater than the heads associated with sea level allowed for infiltration of seawater. Depending on till permeability, infiltrating meltwater is either coming down through the till or is moving laterally under till from the subaerial basalt. Observation of simulated data (not shown) indicates infiltrating meltwater moves into the continental shelf sediments dominantly laterally from the subaerial basalt when till permeabilities are low and dominantly down from the overlying ice sheet when till permeabilities are high. Varying till permeability (within observed ranges) while keeping the continental shelf ice boundary condition at 100% meltwater does little to bring simulated pore fluids at Leg 152 Sites 914–916 closer to observed values (Figure 3b).

4.1.3. Continental Shelf Salinity and δ^{18}O Boundary Conditions

[24] Varying subaerial basalt and till permeabilities within their standard ranges (as discussed in section 3.6) does not produce pore chemistry values consistent with observed values. Inspection of δ^{18}O and salinity pore fluid chemistry revealed that simulated pore fluid chemistry was up to 10 times isotopically lighter than observed values indicated. Changing salinity and δ^{18}O boundary conditions to 0.0315 mass fraction Cl^- and -3‰ δ^{18}O on the continental shelf produced simulated pore fluid chemistry more congruous with Leg 152 data (Figure 3c). We ran the same variation of subaerial basalt permeabilities in SN6–SN8 (Figure 3c) as in SN1–SN3 (Figure 3a), and the boundary condition was the only difference; thus, the fluid dynamics described for SN1–SN3 is the same for SN6–SN8. The till permeability during these simulations was 10^{-17} m^2. Freshening of continental shelf pore fluids occurred during glacial maximums. This implies that infiltrating meltwater comes from above, through the glacial till. The best fit with observed data occurred when basalt permeabilities were moderate ($K_x = 10^{-14}$ m^2).

4.1.4. Subaerial Basalt: Infiltration and Discharge

[25] We plotted subglacial infiltration and SMGD (in volume of flow per unit length of coastline per year) for sensitivity runs SN1–SN3 (Figure 4). Comparison between subglacial infiltration and SMGD shows that they are highly associated with one another and are of the same order of magnitude for each scenario. Generally, as the subaerial basalt horizontal permeability increases from 10^{-14} to 10^{-12} m^2, subglacial infiltration and submarine groundwater discharge increases from $\sim 10^2$ to $\sim 10^4$ m^3 m^{-1} yr^{-1} during glacial maximums (Figure 4). Both the magnitude of SMGD and sub-ice sheet infiltration correlate with ice sheet thickness. The larger the ice sheet is, the greater the SMGD and sub-ice sheet infiltration are.

4.2. BFS Model Results Analysis

[26] Our sensitivity study indicates that the BFS is SN7 (Figure 3c). This scenario has subaerial basalt permeability set at 10^{-14} m^2 and 10^{-15} m^2 in the x and z directions, respectively (Table 3), and has a 93% seawater and 7% meltwater continental shelf ice boundary condition (Figures 5a and 5f). SN7 corresponds to maximum SMGD (during LGM, 22 ka) of 8.33×10^2 m^2 m^{-1} yr^{-1} and present-day SMGD of 8.5×10^1 m^2 m^{-1} yr^{-1} (Figures 6 and 7). During the LGM, lateral groundwater velocities (v_x) within the subaerial basalt were about 10^{-2}–10^{-1} m yr^{-1}, and vertical velocities (v_z) were about 10^{-3}–10^{-2} m yr^{-1} downward. Subaerial basalt v_z shifted to upward flow ($\sim 10^{-3}$–10^{-2} m yr^{-1}) oceanward of the shelf-slope break during the LGM. Subaerial basalt velocity magnitude and direction changed during ice-free conditions, decreasing by 1–2 orders of magnitude and generally shifting upward and landward. Simulated present-day subaerial basalt velocities are of the same order of magnitude as during the ice-free conditions. For present-day conditions, v_z underneath the ice sheet ranges from 10^{-5} m yr^{-1} at the center of the ice sheet to

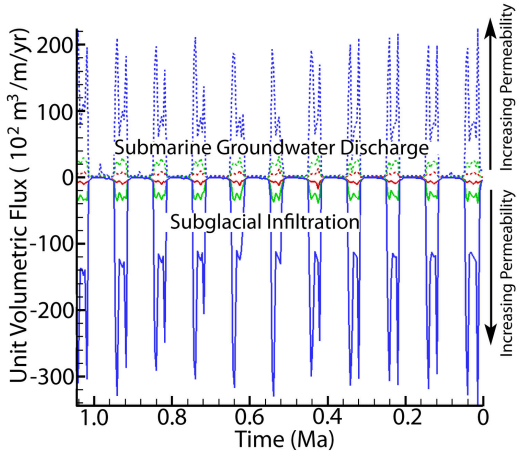

Figure 4. Simulated cumulative subglacial infiltration or recharge (solid lines) and submarine groundwater discharge (dashed lines) from the sensitivity study during the late Pleistocene in which permeability of the subaerial basalt was varied. The fluxes represent volume of water per unit length of coastline per time. Subglacial and submarine groundwater discharge for simulations with different subaerial basalt permeability are presented. Blue line, $K_x = 10^{-12}$ m^2; green line, $K_x = 10^{-13}$ m^2; red line, $K_x = 10^{-14}$ m^2. All models assume anisotropy of 10. Glacial periods occur when submarine groundwater discharge and subglacial infiltration peak.

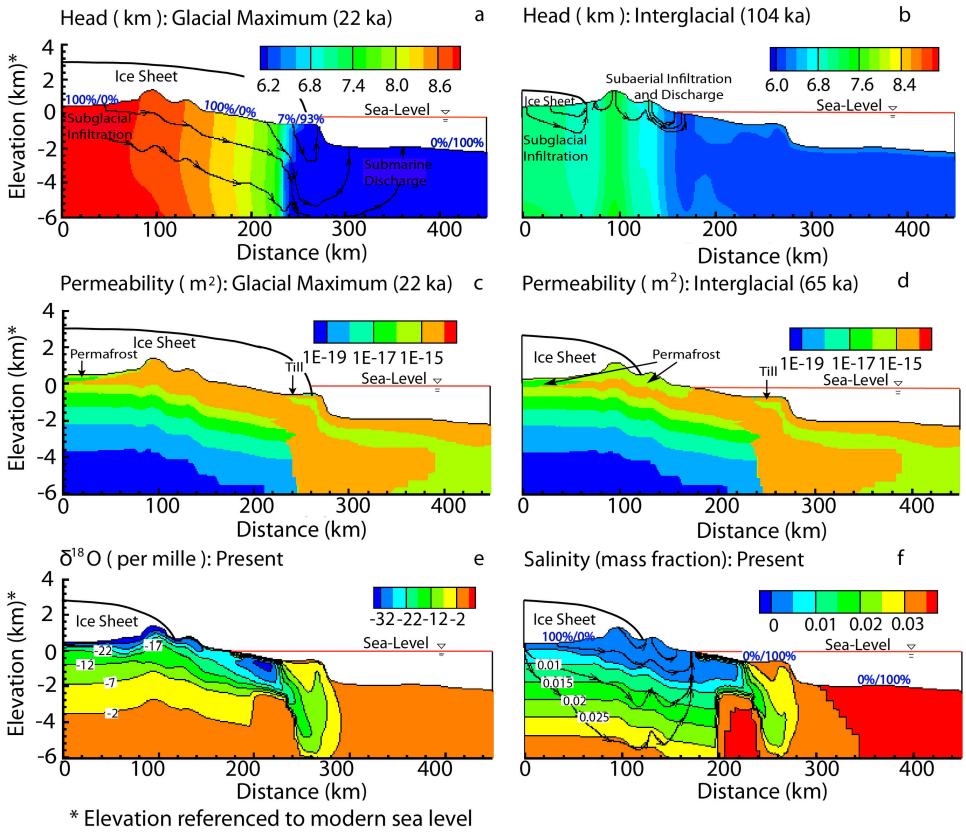

Figure 5. Computed head distribution for (a) the Last Glacial Maximum (LGM) and (b) last interglacial period. Dynamic permeability distribution during (c) the LGM and (d) last interglacial period. Permeability changed because of the presence of permafrost. Present-day (e) $\delta^{18}O$ and (f) solute mass fraction distribution (35 ppt = 0.035 g salinity g^{-1} water). Black arrows in Figures 5a, 5b, and 5f represent dominant streamlines, indicating the direction of flow at a given time. Each plot contains the ice sheet geometry and sea level used for the presented time period. Blue numbers represent the meltwater percent/seawater percent used as a boundary condition at the time described.

10^{-3} m yr^{-1} at the edge of the ice sheet. During the LGM, downward v_z directly underneath the ice sheet increased from 10^{-5} m yr^{-1} at the center of the ice sheet to 10^{-2} m yr^{-1} at the edge of the ice sheet. For both the LGM and present conditions, our model simulates lateral flow under the ice sheet ranging from 10^{-5} m yr^{-1} at the center of the ice sheet to 10^{-1} m yr^{-1} at the ice sheet edge.

[27] The SN7 simulation approached dynamic equilibrium with respect to salinity and $\delta^{18}O$ after about 9 glacial cycles (of the total 10.5 cycles). There is a salinity transition zone within continental shelf sediments, consistent with the pore water data from Leg 152. The salinity transition zone moves seaward during glacial maximums because of increased head gradients caused by ice sheet loading (Figure 5a) and moves back during sea level highstands when seawater infiltrates. Flow is downward on the continental shelf during the LGM (Figure 5a), implying that the ODP well freshening occurred in the past. The calculated pore fluids in the subaerial basalt are dominated by meltwater from the present-day coastline to about 150 km offshore and 5.5 km underneath the continental shelf surface (Figures 5e and 5f). Recharge and discharge on the continental shelf and discharge off the shelf occurred during interglacial periods in ice-free areas (Figure 5d). However, permafrost retarded infiltration rates on the continental shelf when ice sheet thickness was relatively low, such as during interglacials (Figure 5d).

[28] Infiltration and discharge patterns in our model vary in space and time. They consistently have maximum rates in glacial periods (Figures 6 and 7). The model suggests that during glacial periods, groundwater discharge decays logarithmically from the toe of the ice sheet toward the sea (not shown). The location of peak discharge at any time can be subaerial or submarine, depending on the proximity of the ice sheet to the sea (Figures 5a, 5b, and 5f).

[29] The greatest amount of SMGD occurred when the ice sheet is largest (glacial maximums) (Figures 6 and 7). Subglacial infiltration, per unit width of cross section, along the ice sheet length is, on average, 8×10^2 m^3 m^{-1} yr^{-1} during glacial periods (Figure 6) and 0 m^3 m^{-1} yr^{-1} during interglacials (Figure 6); corresponding average SMGD and average subaerial discharges are 8×10^2 and 0.0 m^3 m^{-1} yr^{-1} (Figure 6) during glacial maximums and 7.5×10^1 and 3×10^2 m^3 m^{-1} yr^{-1} during interglacials.

[30] A subsurface hydrologic budget is presented in Figure 7, which is based on the BFS model results. The ice sheet presence can as much as double infiltration on the continental shelf. Simulated present-day infiltration on the continental shelf (including both subaerial and subglacial)

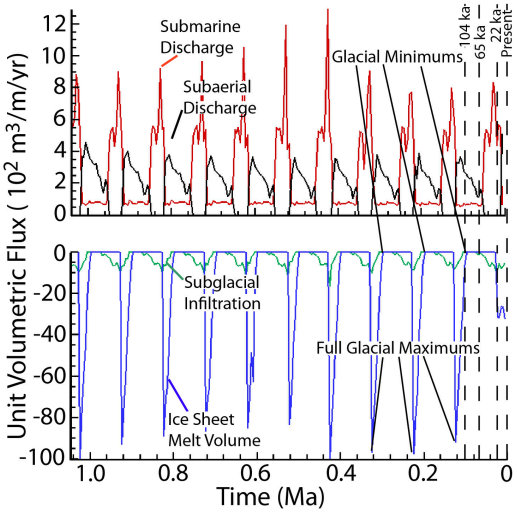

Figure 6. Simulated fluxes (volume per unit length of coastline per time) for the best fit scenario (SN7): Submarine groundwater discharge (red line), subaerial groundwater discharge (black line), ice sheet melt volume (blue line), and subglacial infiltration (green line) volumetric flux for model simulation (1.05 Ma). The points labeled as glacial minimums and full glacial maximums give reference points for all within the simulation; the right side of the ice sheet melt volume peak is the full glacial maximum, and the left side of the peak is the glacial minimum. The positive values indicate discharge, and the negative values represent infiltration. Dashed lines represent time periods presented in Figure 5: 22 ka (Figures 5a and 5c), 104 ka (Figure 5b), 65 ka (Figure 5d), and the present (Figures 5e and 5f).

is 488 $m^3\ m^{-1}\ yr^{-1}$ (Figure 7c), and simulated infiltration (subglacial) during the LGM was 903 $m^3\ m^{-1}\ yr^{-1}$ (Figure 7a). These values are more than 1.5–3 times the infiltration simulated for a period without any ice sheet (307 $m^3\ m^{-1}\ yr^{-1}$; Figure 7b). During the LGM, virtually all subglacial infiltration becomes SMGD; water within the pore fluids (which is likely meltwater during the LGM) is discharged into the ocean and is displaced by meltwater. Simulated discharge during the LGM was almost completely SMGD (870 $m^3\ m^{-1}\ yr^{-1}$; Figure 7a), while simulated subaerial discharge dominated discharge during the ice-free interglacial conditions (306 $m^3\ m^{-1}\ yr^{-1}$; Figure 7b). On the basis of our model simulation present-day subaerial discharge (292 $m^3\ m^{-1}\ yr^{-1}$) is greater than present-day submarine discharge (85 $m^3\ m^{-1}\ yr^{-1}$), supporting the idea that subaerial discharge is the dominant mechanism of groundwater discharge of infiltrated meltwater (Figures 6 and 7c). Comparison between the fluxes of the LGM conditions and the fluxes of the ice-free interglacial conditions clearly indicate that the presence of the ice sheet has a substantial impact on groundwater infiltration and discharge into ocean.

[31] For a glacial retreat the simulated ice sheet decreases in volume by $6 \times 10^8\ m^3\ m^{-1}$. Over the glacial retreat period (25 kyr) the average subglacial infiltration is $2.5 \times 10^7\ m^3\ m^{-1}$, SMGD is $2 \times 10^7\ m^3\ m^{-1}$, and subaerial discharge is $1.4 \times 10^7\ m^3\ m^{-1}$; these factors represent 4.4%, 3.8%, and 2.4% of ice sheet melting during the glacial retreat, respectively.

5. Discussion

[32] The simulated groundwater flow patterns have important implications for locations of upward seepage of groundwater, sea level rise, and present and past continental biochemical processes. Computed upwelling of groundwater occurred dominantly just beyond the edge of the ice sheet and (according to our model) should be occurring at present in SE Greenland. This implies groundwater is exiting near the margin of the ice sheet through taliks or along meltwater streams where permafrost is present. These groundwater springs could have the chemical signature of water in equilibrium with the underlying geology, paleomeltwater, or meltwater sourced from ice closer to the ice sheet summit. *McIntosh et al.* [2002] noted that infiltration of glacial meltwaters within the Michigan basin promoted microbiological reactions in organic-rich shale deposits, leading to the generation of economically significant quantities of natural gas. Our model results suggest that freshwater inputs could be contributing to microbial processes on Greenland's continental shelf.

[33] During glacial maximums, computed submarine discharge is substantially greater than submarine infiltration (Figure 7a). Submarine discharge is occurring up to 300 km off the continental shelf-slope break. Glacial meltwater coming from mountain glaciers along the Gulf of Alaska contained high bioavailable dissolved organic carbon (DOC) and older ^{14}C ages compared to stream water [*Hood et al.*, 2009]. This suggests that during the LGM and older glacial maximums, substantial amounts of bioavailable DOC was discharging into the ocean up to about 300 km off the continental shelf. This occurrence could have past and future impacts on the biogeochemistry of coastal ecosystems [*Hood et al.*, 2009].

[34] One important component to future sea level rise is the melting of Greenland ice sheet; the near-complete melting of the Greenland ice sheet during the Eemian interglacial might have contributed 4–5.5 m of sea level rise [*Cuffey and Marshall*, 2000]. For a permeability range of 10^{-14}–$10^{-13}\ m^2$, our model estimates that an average of ~1%–4% of ice sheet meltwater during a glacial retreat is represented by SMGD in SE Greenland. The influence of modern SMGD is less significant than during the LGM because of the size and proximity of the ice sheet to the shore. Our model shows that for current conditions, subaerial groundwater discharge dominates along our cross section, though the discharge converges right along the shoreline (Figures 5f, 6, and 7). However, our BFS predicts that SMGD is occurring today, at rates of 85 $m^3\ m^{-1}\ yr^{-1}$ along our cross section (Figure 7c). A rough calculation indicates that this would represent $\sim 3 \times 10^{10}\ m^3\ yr^{-1}$ if applied to all of Greenland (multiply by circumference of 39,330 km), which is 11% of Greenland's estimated melt rate ($27.8 \times 10^{10}\ m^3\ yr^{-1}$) from meltwater runoff between 1961 and 1990 [*Hanna et al.*, 2005]. This value shows that submarine discharge of ice sheet meltwater is potentially an important, yet unquantified, mechanism transporting meltwater to the ocean and thus requires more study and attention. Of course, it is hard to quantify how much of the discharge is past and present ice sheet meltwater. Further, SMGD of ice sheet meltwater is likely greater to the north, where there are larger areas of surface-exposed permeable

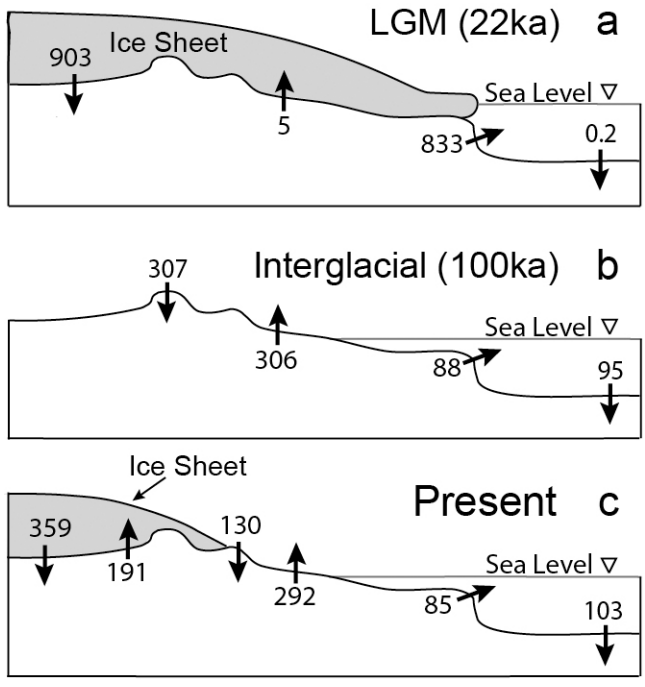

Figure 7. Simulated subsurface hydrologic budget for SE Greenland: computed groundwater flux ($m^3 yr^{-1}$), infiltration (down arrows) and discharge (up arrows), during (a) the LGM (22ka), (b) the interglacial (100 ka in our model), and (c) the present. All numbers are per unit width of the cross section. Arrows under the ice sheet represent subglacial flux (infiltration and/or discharge), arrows under the ocean represent submarine flux, and arrows under neither the ocean nor the ice sheet represent subaerial flux. Note that fluxes likely do not represent steady state conditions.

subaerial basalt [*Larsen et al.*, 1998]. This could also be a dominant mechanism of transporting nutrients to coastal waters in areas lacking river outflow.

[35] Our model shows that the emplacement and extent of fresh, isotopically light water into SE Greenland's continental shelf and adjacent ocean could be influenced by head gradients induced by thick ice sheets and the distribution of permeability of underlying rocks and sediments. Throughout the glacial cycle, cold surface conditions produced permafrost, particularly under the center of thick ice sheets, under the edges of the ice sheets, and at subaerially exposed geological surfaces (Figures 2b, 2c, 5c, and 5d). During glacial periods the ice sheet had an insulating effect, producing less permafrost than during the interglacials [*Marshall and Clark*, 2002; *Tarasov and Peltier*, 2007] (Figures 2b, 2c, 5c, and 5d). During the LGM, the ice sheet reduced permafrost lateral extent by as much as 100 km compared to times with no ice sheet.

[36] The subaerial basalt unit was the main aquifer contributing to offshore freshwater (Figures 1c and 5d–5f). The subaerial basalt is exposed to the land surface; it is covered by ice during glacial maximums and is partially covered by seawater during interglacials. The subaerial basalt focuses ice sheet meltwater offshore and into continental shelf sediments. These subaerial basalts have greater aerial exposure to the north of our cross section [*Larsen et al.*, 1998], and thus potentially higher meltwater infiltration rates into the groundwater may have occurred there.

[37] Modern basal melting rate in Greenland is conservatively estimated as 0.006 m yr^{-1} [*Hooke and Fastook*, 2007]. In contrast, the average modern subglacial infiltration rate across our cross section is 0.001 m yr^{-1}. It is possible that because of the present size of the ice sheet in SE Greenland, only a portion of the basal meltwater infiltrates into the groundwater through low-permeability locations. Recent studies show surface meltwater draining to the base of the ice sheet via fractures or moulins [*Joughin et al.*, 2008]. The surface meltwater could infiltrate into the groundwater along with basal meltwater in high-permeability locations. Our simulated infiltration rate is comparable to the values computed for the North American craton during the last glaciation, which ranged between 0 and 0.006 m yr^{-1}, though mostly it was around 0.002 m yr^{-1}. *Lemieux et al.* [2008] used prescribed fluxes dictated by changing ice sheet size and set the flux to zero in areas underneath the ice sheet that were not near the ice floatation level. The prescribed flux method requires assumptions about recharge, such as assuming all meltwater over a period infiltrates. Such an assumption could have a tendency to increase infiltration rates. However, greater infiltration rates calculated by *Lemieux et al.* [2008] were likely a result of less permafrost underneath the ice sheet and overall greater permeability. It is important to note that surface melting rates in western Greenland are highly spatially and temporally variable, ranging between 0 and 24 m yr^{-1} [*van den Broeke et al.*, 2008]. A highly idealized model like ours does not include this kind of variability.

[38] As pointed out in section 4, the greatest factor affecting the calculated continental shelf $\delta^{18}O$ and Cl^- concentrations of the pore fluids was the concentration boundary conditions on the continental shelf during glacial maximums. We fixed the sub-ice sheet concentration and

isotopic composition to be ~7% meltwater and ~93% seawater, respectively, when continental shelf nodes were covered by the ice sheet, instead of 100% meltwater. Simulations that assumed 100% meltwater beneath continental shelf nodes caused the calculated concentrations of $\delta^{18}O$ and Cl^- concentrations to be substantially fresher and isotopically lighter than measured values (Figures 1a and 1b). A number of prior studies report $\delta^{18}O$ values of basal ice and meltwater to be isotopically heavier than excepted [*Knight*, 1987; *Ma et al.*, 2004; *Siegel*, 1991; *Souchez et al.*, 1990]. Laurentide ice sheet glacial meltwater in the midcontinent of the United States has $\delta^{18}O$ up to −9‰, presumably because of isotopically heavy Pleistocene ice and meltwater [*Ma et al.*, 2004; *Siegel*, 1991]. Isotopic exchange with debris may also act to increase the $\delta^{18}O$ of melting ice water. However, these processes will not account for our need to alter the salinity boundary condition. Figure 1b clearly illustrates that the pore fluids found at Sites 914–916 are mixtures of seawater and meltwater. A variety of processes could account for the mixture, typically requiring interaction between the ice sheet and seawater. Ice forming on the edge of the ice sheet could incorporate seawater, producing ice with chemical signatures similar to sea ice. Sea ice in the Weddell Sea of Antarctica ranged between ~3‰ and ~−20‰ $\delta^{18}O$ and 2 and 0.030 mass fraction salinity because of a mixture of sea ice and meteoric ice [*Lange et al.*, 1990]. Incorporation of seawater could be a result of direct contact between the ice and the seawater during glacial maximums. During winter months, when liquid water within the ice sheet freezes, seawater intrusion into the ice sheet edge is more probable because of stalled ice sheet melting. Waxing and waning of the ice sheet across the shelf with multiple advances and retreats would further cause mixing. Another likely scenario is that at times the ice sheet on the continental shelf was not grounded during glacial maximums.

[39] This modeling study would have benefited from additional pore water data from greater depths along Greenland's continental shelf. Data from greater depths would improve our understanding of the extent of the freshwater plume and the mechanisms for emplacement of isotopically light water. Planning is underway by a consortium of Canadian and Finnish researchers to drill through the Greenland ice sheet, which may provide further insight into subsurface hydrology [*Makahnouk et al.*, 2009].

6. Conclusion

[40] Continental-scale hydrogeologic simulation of SE Greenland indicates that complex interactions between the ice sheet, subsurface geology, and sea level existed during the Pleistocene. These interactions influenced the rate and distribution of infiltration and discharge. In general, the location of the ice sheet edge dictated the location of groundwater discharge. Typically, discharge concentrated just beyond the edge of the ice sheet. Our sensitivity study emphasizes the importance of the permeable subaerial basalt in acting as a conduit to focus water offshore and how the presence of the ice sheet played a significant role in SMGD. During the Last Glacial Maximum, SMGD likely occurred up to many hundreds of kilometers offshore, potentially having a significant effect on the marine ecosystems. Our model further supports the concept of movement of ice meltwater through the subsurface to the ocean, and present occurrences should be given more attention. Ice sheet–derived SMGD represents between about 1% and 4% of Greenland's total ice sheet melting.

Appendix A: Numerical Methods

A1. Groundwater Flow

[41] We solved for variable density groundwater flow using

$$\nabla \cdot \left[\mathbf{K}\mu_r\rho_f\nabla(h+\rho_r z)\right] = S_s\rho_0\left[\frac{\partial h}{\partial t} - \frac{\partial \eta}{\partial t}\frac{\rho_i}{\rho_w}\right], \tag{A1}$$

where $\mathbf{K}$ is the hydraulic conductivity tensor, h is the hydraulic head, ρ_0 is the water density at standard conditions (10°C, 0.0 mass fraction salinity, and 0.0 MPa), ρ_r is the relative density, μ_r is the water viscosity, S_s is the specific storage, ρ_f is the density of groundwater, t is time, η is the thickness of the ice sheet, ρ_w is the density of water, and ρ_i is the density of ice. We represent ice sheet loading with the second term on the right-hand side of equation (A1), which has a loading efficiency of 1. Freshwater hydraulic head in equation (A1) is given by

$$h = \frac{P}{\rho_0 g} + z, \tag{A2}$$

where P is fluid pressure, g is gravitational acceleration, and z is elevation above reference datum [*Hubbert*, 1940]. Equation (A1) can account for anomalous pore pressures in low-permeability confining units caused by ice sheet loading.

[42] We used the following equation for the variable density form of Darcy's law in our model [*Garven and Freeze*, 1984]:

$$\mathbf{q} = -\mathbf{K}\mu_r\nabla(h+\rho_r z). \tag{A3}$$

[43] The relative density (ρ_r) and viscosity (μ_r) used in equations (A1) and (A3) are given by

$$\rho_r = \frac{\rho_f - \rho_0}{\rho_0} \tag{A4}$$

$$\mu_r = \frac{\mu_0}{\mu_f}, \tag{A5}$$

where μ_0 is the viscosity of water at standard conditions (10°C, 0.0 MPa, and 0.0 mass fraction salinity) and μ_f is the viscosity of water.

[44] The principle components of the hydraulic conductivity tensor $\mathbf{K}$ are in the x and the z directions. Components K_{xx}, K_{zz}, K_{zx}, and K_{xz} are calculated using

$$\begin{aligned} K_{xx} &= K_{\max}\cos^2(\theta) + K_{\min}\sin^2(\theta), \\ K_{zz} &= K_{\max}\sin^2(\theta) + K_{\min}\cos^2(\theta), \\ K_{xz} &= K_{zx} = (K_{\max} - K_{\min})\sin(\theta)\cos(\theta), \end{aligned} \tag{A6}$$

where θ is the dip of the layering, $K_{\max}$ is the maximum (layer-parallel) hydraulic conductivity, $K_{\min}$ is the minimum

(layer-normal) hydraulic conductivity, and dip is measured relative to horizontal. In our model, we assumed the geologic units to be composed of flat lateral units, resulting in $\theta = 0$. This means $K_{xx} = K_{\max}$ and $K_{zz} = K_{\min}$ and $K_{xz} = K_{zx} = 0$.

A2. Solute Transport

[45] We used the following equation to represent advective-dispersive solute transport [*Freeze and Cherry*, 1979]:

$$\nabla \cdot [\mathbf{D}\nabla C] - \mathbf{v} \cdot \nabla C = \frac{\partial C}{\partial t}, \tag{A7}$$

where $\mathbf{D}$ is the hydraulic dispersion-diffusion tensor, $\mathbf{v}$ is the groundwater velocity ($\mathbf{v} = \mathbf{q}/\phi$), ϕ is porosity, and C is species concentration. In this present application, we model the total dissolved solids concentration, reported as mass fraction (kilograms of salt per kilograms of solution). Equation (A7) neglects the effects of solute diffusion into low-permeability blocks and rapid advective transport through fractures. Equation (A7) also neglects fluid-rock geochemical reactions at depth. Computed salinity units are in solute mass fraction but have been converted to mM chlorinity for Figure 2. The tensor $\mathbf{D}$ has four components, D_{xx}, D_{zz}, D_{zx}, and D_{xz}, defined by

$$\begin{aligned} D_{xx} &= \frac{\nu_x^2}{|\mathbf{v}|}\alpha_L + \frac{\nu_z^2}{|\mathbf{v}|}\alpha_T + D_d, \\ D_{zz} &= \frac{\nu_z^2}{|\mathbf{v}|}\alpha_L + \frac{\nu_x^2}{|\mathbf{v}|}\alpha_T + D_d, \\ D_{xz} &= D_{zx} = (\alpha_L - \alpha_T)\frac{\nu_x \nu_z}{|\mathbf{v}|}, \end{aligned} \tag{A8}$$

where x and z are components of seepage velocity in the x and z directions ($\nu_x = q_x/\phi$ and $\nu_z = q_z/\phi$), D_d is the diffusion coefficient, and $|\mathbf{v}|$ is

$$|\mathbf{v}| = \sqrt{\nu_x^2 + \nu_x^2}. \tag{A9}$$

A3. The ^{18}O Transport

[46] Fluid-rock isotope exchange reactions can generally be neglected when temperatures are less than 150°C [*Bowman et al.*, 1994]. This was the case for our hydrologic models of Greenland; temperature at the base of our model never exceeded 90°C. We used ^{18}O transport equations identical to equations (A7)–(A9):

$$\nabla \cdot \left[\mathbf{D}\nabla R_f\right] - \mathbf{v} \cdot \nabla R_f = \frac{\partial R_f}{\partial t}, \tag{A10}$$

where R_f is the fluid $^{18}O/^{16}O$ ratio. We report $\delta^{18}O$ results and observations in units of per mil.

A4. Heat Transport

[47] Temperature can affect fluid density and permafrost distribution in our model. Our code solves a conductive and convective-dispersive heat transfer equation:

$$\left[c_f \rho_f \phi + c_s \rho_s (1-\phi)\right]\frac{\partial T}{\partial t} = \nabla \cdot [\lambda \nabla T] - \mathbf{q} \cdot \left[\rho_f c_f \nabla T\right], \tag{A11}$$

where λ is the thermal dispersion-conduction tensor, ϕ is porosity, T is temperature, c_s and c_f are the specific heat capacities of the solid and liquid phases, respectively, and ρ_s is the density of the solid phase. Permafrost can have an important effect on subsurface permeability [*McKenzie et al.*, 2007]. When temperatures were below the pressure melting point, we lowered permeability by 2 orders of magnitude. We neglected latent heat of fusion associated with freezing/thawing in equation (A11). *Bense and Person* [2008] found that the latent heat of melting could delay permafrost thawing by a few thousand years. On the time scale of a glacial cycle (100 kyr) the effects of neglecting this should be small. The tensor has the form

$$\begin{aligned} \lambda_{xx} &= \rho_f c_f \frac{q_x^2}{|\mathbf{q}|}\alpha_L + \frac{q_z^2}{|\mathbf{q}|}\alpha_T + \lambda_f^{\phi}\lambda_s^{1-\phi}, \\ \lambda_{zz} &= \frac{q_x^2}{|\mathbf{q}|}\alpha_T + \rho_f c_f \frac{q_z^2}{|\mathbf{q}|}\alpha_L + \lambda_f^{\phi}\lambda_s^{1-\phi}, \\ \lambda_{xz} &= \lambda_{zx} = (\alpha_L - \alpha_T)\frac{q_x q_z}{|\mathbf{q}|}\rho_f c_f, \end{aligned} \tag{A12}$$

where λ_{xx}, λ_{zz}, λ_{xz}, and λ_{zx} are the tensor components, α_T and α_L are the transverse and longitudinal thermal dispersivities, respectively, and q_x and q_z are the Darcy fluxes in the x and z directions. Here λ_f and λ_s are the thermal conductivities of the fluid and solid phases, respectively, which are assumed to be isotropic and scalar quantities; q is the absolute value of the Darcy flux, which is given by

$$|\mathbf{q}| = \sqrt{q_x^2 + q_x^2}. \tag{A13}$$

A5. Equations of State

[48] Thermodynamic equations of state are used to compute the density and viscosity of groundwater at elevated temperature, pressure, and salinity conditions. Our code uses the polynomial expressions of *Kestin et al.* [1981]:

$$\begin{aligned} \frac{1}{\rho_f} = {} & a(T) + b(T)P + c(T)P^2 + Cd(T) + C^2 e(T) \\ & - PCf(T) - C^2 Pg(T) - \frac{h(T)}{2}P^2, \end{aligned} \tag{A14}$$

$$\mu_f = \mu_0[1 + B(T,C)P], \tag{A15}$$

where $a(T)$, $b(T)$, . . . , $h(T)$, and $B(T,C)$ are third-and fourth-order temperature-and concentration-dependent polynomials. These polynomial expressions are valid for temperatures between 10°C and 150°C and salinities between 0 and 6 M NaCl. Fluid density is more sensitive to temperature and salinity than fluid pressure. Below 10°C, we set viscosity and fluid density to standard state conditions (10°C).

Appendix B: Analytical Solutions—Basal Ice Sheet Temperature

[49] We used the following analytical solution to calculate the temperature at the base of the ice sheet. In the

accumulation zone of the ice sheet we used the following convective-conductive transport equation [*Hooke*, 1998]:

$$T_i(z_i) = T_s - \frac{\sqrt{\pi}}{2}\frac{\beta_o}{\zeta}[\mathrm{erf}(\zeta\eta) - \mathrm{erf}(\zeta z_i)], \tag{B1}$$

$$\zeta^2 = \sqrt{\frac{w}{2\kappa\eta}}, \tag{B2}$$

$$\mathrm{erf}(s) = \frac{1}{\sqrt{2\pi}}\int_0^s e^{-\frac{t^2}{2}}\mathrm{d}t, \tag{B3}$$

where z_i is the elevation above the base of the ice sheet, T_s is the surface temperature of the ice sheet, β_o is the basal temperature gradient, η is the thickness of the ice sheet, κ is the ice thermal diffusivity, w is the vertical ice velocity at the ice surface, and b_n is the net accumulation rate. Here w is set to equal b_n. We assumed the vertical velocity at the base of the ice sheet was insignificant ($\sim$0 m yr^{-1}). In the ablation zone the flowing variation of equation (B1) is used:

$$T_i(z_i) = T_s - \frac{\sqrt{\pi}}{2}\frac{\beta_o}{\zeta}[\chi(\zeta\eta) - \chi(\zeta z_i)], \tag{B4}$$

$$\chi(s) = \frac{1}{\sqrt{2\pi}}\int_0^s e^{\frac{t^2}{2}}\mathrm{d}t. \tag{B5}$$

[50] We set T_s to equal the air temperature. In instances where the calculated basal temperature was higher than the pressure melting temperature (T_{pmp}) we set basal temperature to T_{pmp} (Figures 2b and 2c),

$$T_{\mathrm{pmp}} = T_{\mathrm{TP}} - c_i\rho_i g H, \tag{B6}$$

where T_{TP} is the triple point temperature, c_i is the depression of the melting point of water with increased pressure, ρ_i is the density of ice, g is gravity, and H is the thickness of the ice sheet.

[51] We approximated net snow accumulation rate (b_n) at the summit by assuming a linearly temperature-dependent accumulation rate, determined from data presented by *Cuffey and Clow* [1997]:

$$b_n = 0.0085 z_i + 0.4845. \tag{B7}$$

[52] Then we calculated b_n across the ice sheet by having b_n decrease linearly down the ice sheet, crossing zero midway down; the transition point between the accumulation and ablation zones occurred at the point along the ice sheet in which the thickness of the ice sheet was half of the thickness of the ice sheet at the summit. Note that b_n is negative in the ablation zone of the ice sheet, where the ice is sublimating and melting.

[53] **Acknowledgments.** The maps in Figure 1 were created using Generic Mapping Tools, created by *Wessel and Smith* [1990]. This work was supported by an NSF ocean science grant OCE-0824263 to Brandon Dugan, Mark Person, and Dan Lizarralde.

References

Bense, V. F., and M. A. Person (2008), Transient hydrodynamics within intercratonic sedimentary basins during glacial cycles, *J. Geophys. Res.*, *113*, F04005, doi:10.1029/2007JF000969.

Bowman, J. R., S. D. Willett, and S. J. Cook (1994), Oxygen isotopic transport and exchange during fluid flow: One-dimensional models and applications, *Am. J. Sci.*, *294*, 1–55.

Cohen, D., et al. (2009), Origin and extent of fresh paleowaters on the Atlantic continental shelf, USA, *Ground Water*, *48*, 143–158.

Cuffey, K. M., and G. D. Clow (1997), Temperature, accumulation, and ice sheet elevation in central Greenland through the last deglacial transition, *J. Geophys. Res.*, *102*, 26,383–26,396, doi:10.1029/96JC03981.

Cuffey, K. M., and S. J. Marshall (2000), Substantial contribution to sea-level rise during the last interglacial from the Greenland ice sheet, *Nature*, *404*, 591–594.

Dahl-Jensen, D., K. Mosegaard, N. Gundestrup, G. D. Clow, S. J. Johnsen, A. W. Hansen, and N. Balling (1998), Past temperatures directly from the Greenland ice sheet, *Science*, *282*, 268–271.

Engelhardt, H., and B. Kamb (1997), Basal hydraulic systems of a West Antarctic ice stream: Constraints from borehole observations, *J. Glaciol.*, *43*, 207–230.

Fisher, A. T. (1998), Permeability within basaltic oceanic crust, *Rev. Geophys.*, *36*, 143–182, doi:10.1029/97RG02916.

Fisher, A. T., E. E. Davis, and K. Becker (2008), Borehole-to-borehole hydrologic response across 2.4 km in the upper oceanic crust: Implications for crustal-scale properties, *J. Geophys. Res.*, *113*, B07106, doi:10.1029/2007JB005447.

Flowers, G., S. Marshall, H. Bjornsson, and G. Clarke (2005), Sensitivity of Vatnajokull ice cap hydrology and dynamics to climate warming over the next 2 centuries, *J. Geophys. Res.*, *110*, F02011, doi:10.1029/2004JF000200.

Freeze, R. A., and J. A. Cherry (1979), *Groundwater*, Prentice Hall, Englewood Cliffs, N. J.

Garven, G., and R. A. Freeze (1984), Theoretical analysis of the role of groundwater flow in the genesis of stratabound ore deposits; 1, Mathematical and numerical model, *Am. J. Sci.*, *284*, 1085–1124.

Gerber, R. E., and K. Howard (2000), Recharge through a regional till aquitard: Three-dimensional flow model water balance approach, *Ground Water*, *38*, 410–422.

Gieskes, J. M., D. Schrag, L. Chan, L. Zhang, and R. W. Murray (1998), Geochemistry of interstitial waters, *Proc. Ocean. Drill. Program Sci. Results*, *152*, 293–305.

Gingerich, S. B. (1999), Estimating transmissivity and storage properties from aquifer tests in the southern Lihue Basin, Kauai, Hawaii, *U.S. Geol. Surv. Water Resour. Invest. Rep. 99-4066*.

Hanna, E., P. Huybrechts, I. Janssens, J. Cappelen, K. Steffen, and A. Stephens (2005) Runoff and mass balance of the Greenland Ice Sheet: 1958–2003, *J. Geophys. Res.*, *110*, D13108, doi:10.1029/2004JD005641.

Hood, E., J. Fellman, R. G. M. Spencer, P. J. Hernes, R. Edwards, D. D'Amore, and D. Scott (2009), Glaciers as a source of ancient and labile organic matter to the marine environment, *Nature*, *462*, 1044–1047.

Hooke, R. L. (1998), *Principles of Glacier Mechanics*, Prentice Hall, Upper Saddle River, N. J.

Hooke, R. L., and J. Fastook (2007), Thermal conditions at the bed of the Laurentide ice sheet in Maine during deglaciation: Implications for esker formation, *J. Glaciol.*, *53*, 646–658.

Hooyer, T. S., and N. R. Iverson (2002), Flow mechanism of the Des Moines lobe of the Laurentide ice sheet, *J. Glaciol.*, *48*, 575–587.

Hopper, J. R., T. Dahl-Jensen, W. S. Holbrook, H. C. Larsen, D. Lizarralde, J. Korenaga, G. M. Kent, and P. B. Kelemen (2003), Structure of the SE Greenland margin from seismic reflection and refraction data: Implications for nascent spreading center subsidence and asymmetric crustal accretion during North Atlantic opening, *J. Geophys. Res.*, *108*(B5), 2269, doi:10.1029/2002JB001996.

Hubbert, M. K. (1940), The theory of groundwater motion, *J. Geol.*, *48*, 785–944.

Imbrie, J., J. Hays, D. Martinson, A. McIntyre, A. C. Mix, J. Morley, N. G. Pisias, W. L. Prell, and N. J. Shackleton (1984), The orbital theory of Pleistocene climate: Support from a revised chronology of the marine δ^{18}O record, in *Milankovitch and Climate*, pp. 269–305, D. Reidel, Boston, Mass.

Ingebritsen, S. E., and C. E. Manning (1999), Geological implications of a permeability-depth curve for the continental crust, *Geology*, *27*, 1107–1110.

Izuka, S. K., and S. B. Gingerich (2003), A thick lens of fresh groundwater in the southern Lihue Basin, Kauai, Hawaii, USA, *Hydrogeol. J.*, *11*, 240–248.

Johnsen, S. J., T. Dahl-Jensen, W. Dansgaard, and N. Gundestrup (1995), Greenland palaeotemperatures derived from GRIP bore hole temperature and ice core isotope profiles, *Tellus, Ser. B*, *47*, 624–629.

Joughin, I., S. B. Das, M. A. King, B. E. Smith, I. M. Howat, and T. Moon (2008), Seasonal speedup along the western flank of the Greenland ice sheet, *Science*, *320*, 781–778.

Keller, C. K., G. van der Kamp, and J. A. Cherry (1989), A multiscale study of the permeability of thick clayey till, *Water Resour. Manage.*, *25*, 2299–2317.

Kestin, J., H. E. Khalifa, and R. J. Correia (1981), Tables of the dynamic and kinematic viscosity of aqueous NaCl solutions in the temperature range 20–150°C and the pressure range 0.1–35 MPa, *J. Phys. Chem. Ref. Data*, *10*, 71–87.

Knight, P. G. (1987), Observations at the edge of the Greenland ice sheet: Boundary condition implications for modelers, *J. Glaciol.*, *19*, 591–612.

Lange, M. A., P. Schlosser, S. F. Ackley, P. Wadhams, and G. S. Dieckmann (1990), ^{18}O concentrations in sea ice of the Weddell Sea, Antarctica, *J. Glaciol.*, *36*, 315–323.

Larsen, H. C., T. Dahl-Jensen, and J. R. Hopper (1998), Crustal structure along the Leg 152 drilling transect, *Proc. Ocean Drill. Program Sci. Results*, *152*, 463–475.

Le Brocq, A., A. Payne, M. Siegert, and R. Alley (2009), A subglacial water-flow model for West Antarctica, *J. Glaciol.*, *55*, 879–888.

Lemieux, J.-M., E. A. Sudicky, W. R. Peltier, and L. Tarasov (2008), Dynamics of groundwater recharge and seepage over the Canadian landscape during the Wisconsinian glaciation, *J. Geophys. Res.*, *113*, F01011, doi:10.1029/2007JF000838.

Ma, L., M. C. Castro, and C. M. Hall (2004), A late Pleistocene–Holocene noble gas paleotemperature record in southern Michigan, *Geophys. Res. Lett.*, *31*, L23204, doi:10.1029/2004GL021766.

Makahnouk, M., E. Henkemans, S. Frape, T. Ruskeeniemi, P. Lintinen, and M. Hobbs (2009), Geochemical and isotopic characterization of surface and groundwater from an area of continuous permafrost adjacent to the Greenland ice sheet, Kangerlussuaq, Greenland, *Geol. Soc. Am. Abstr. Programs*, *41*(7), 699.

Marshall, S. J., and P. U. Clark (2002), Basal temperature evolution of North American ice sheets and implications for the 100-kyr cycle, *Geophys. Res. Lett.*, *29*(24), 2214, doi:10.1029/2002GL015192.

McIntosh, J. C., L. M. Walter, and A. M. Martini (2002), Pleistocene recharge to midcontinent basins: Effects on salinity structure and microbial gas generation, *Geochim. Cosmochim. Acta*, *66*, 1681–1700.

McKenzie, J. M., C. I. Voss, and D. I. Siegel (2007), Groundwater flow with energy transport and water-ice phase change: Numerical simulations, benchmarks, and application to freezing in peat bogs, *Adv. Water Resour.*, *30*, 966–983.

Norton, D., and H. P. Taylor (1979), Quantitative simulation of the hydrothermal systems of crystallizing magmas on the basis of transport theory and oxygen isotope data: An analysis of Skaergaard intrusion, *J. Petrol.*, *20*, 421–486.

Parizek, B. R., and R. B. Alley (2004), Implications of increased Greenland surface melt under global-warming scenarios: Ice-sheet simulations, *Quat. Sci. Rev.*, *23*, 1013–1027.

Person, M., B. Dugan, J. B. Swenson, L. Urbano, C. Stott, J. Taylor, and M. Millett (2003), Pleistocene hydrogeology of the Atlantic continental shelf, New England, *Geol. Soc. Am. Bull.*, *115*, 1324–1343.

Person, M., J. McIntosh, V. Bense, and V. H. Remenda (2007), Pleistocene hydrology of North America: The role of ice sheets in reorganizing groundwater flow systems, *Rev. Geophys.*, *45*, RG3007, doi:10.1029/2006RG000206.

Siegel, D. I. (1991), Evidence for dilution of deep, confined groundwater by vertical recharge of isotopically heavy Pleistocene water, *Geology*, *19*, 433–436.

Souchez, R., M. Lemmens, R. Lorrain, J.-L. Tison, J. Jouzel, and D. Sugden (1990), Influence of hydroxyl-bearing minerals on the isotopic composition of ice from the basal zone of an ice sheet, *Nature*, *345*, 244–246.

Souza, W. R., and C. I. Voss (1987), Analysis of an anisotropic coastal aquifer system using variable-density flow and solute transport simulation, *J. Hydrol.*, *92*, 17–41.

Spinelli, G. A., E. R. Giambalvo, and A. T. Fisher (2004), Sediment permeability, distribution, and influence on fluxes in oceanic basement, in *Hydrogeology of the Oceanic Lithosphere*, edited by E. E. Davis and H. Elderfield, pp. 151–188, Cambridge Univ. Press, Cambridge, U. K.

Talbot, C. J. (1999), Ice ages and nuclear waste isolation, *Eng. Geol.*, *52*, 177–192.

Tarasov, L., and W. R. Peltier (2007), Coevolution of continental ice cover and permafrost extent over the last glacial-interglacial cycle in North America, *J. Geophys. Res.*, *112*, F02S08, doi:10.1029/2006JF000661.

van den Broeke, M., P. Smeets, J. Ettema, C. van der Veen, R. van de Wal, and J. Oerlemans (2008), Partitioning of melt energy and meltwater fluxes in the ablation zone of the west Greenland ice sheet, *Cryosphere*, *2*, 179–189.

Vialov, S. S. (1958), Regularities of glacial shields movement and the theory of plastic viscous flow, *IAHS Publ.*, *47*, 266–275.

Wessel, P., and W. H. F. Smith (1991), Free software helps map and display data, *Eos Trans., AGU*, *72*(41), 441.

D. Cohen, Department Geological and Atmospheric Science, Iowa State University, 253 Science-1, Ames, IA 50011, USA.

W. DeFoor and M. Person, Hydrology Program, Department of Earth and Environmental Science, New Mexico Institute of Mining and Technology, 801 Leroy Pl., Socorro, NM 87801, USA. (wdefoor@nmt.edu)

B. Dugan, Department of Earth Science, Rice University, 6100 Main St., Houston, TX 77005, USA.

H. C. Larsen, Office of Liaison and Cooperative Research, Integrated Ocean Drilling Program, Inc., Tokyo University of Marine Science and Technology, 3rd Floor, 2-l-6, Etchujima, Koto-ku, Tokyo 135-1855, Japan.

D. Lizarralde, Department of Geology and Geophysics, Woods Hole Oceanographic Institution, 266 Woods Hole Rd., Woods Hole, MA 02543, USA.